

Effect of Ultrasonic Vibration Solidification Treatment on the Corrosion Behavior of AZ80 Magnesium Alloy

Tao Sun¹, Zhongyi Wang¹, Jian Li², Tao Zhang^{2,3,*}

¹ College of Power and Energy Engineering, Harbin Engineering University, Nantong ST 145, Harbin, 150001, China

² Corrosion and protection Laboratory, Key Laboratory of Superlight Materials and Surface Technology (Harbin Engineering University), Ministry of Education, Nantong ST 145, Harbin, 150001, China

³ State Key Laboratory for Corrosion and Protection, Institute of Metal Research, Chinese Academy of Sciences, Wencui RD 62, Shenyang, 110016, China)

*E-mail: zhangtao@hrbeu.edu.cn

Received: 1 November 2012 / Accepted: 13 December 2012 / Published: 1 May 2013

The effects of ultrasonic vibration solidification treatment (UVST) on the corrosion behavior of AZ80 magnesium alloy have been investigated by means of microscopy observations and electrochemical measurements. The results show that the UVST process improves the corrosion resistance of AZ80 alloy. The electrochemical noise results analyzed by recurrence plots reveal that the AZ80-UVST alloy shows the lower corrosion initiation rate and growth probability than normal solidification alloy (AZ80-NS alloy). These observations have been explained from point of view of microstructure changes, wherein the significant decrease of twins and dislocation inhibits the corrosion initiation rate and the refined β phase decreased the corrosion growth probability of AZ80-UVST alloy.

Keywords: ultrasonic vibration solidification; magnesium; TEM; electrochemical noise; recurrent plots

1. INTRODUCTION

Among the light metals, magnesium presents very interesting engineering properties owing to its high specific rigidity, high thermal conductivity, biocompatibility and easy recycling. These properties make magnesium very attractive for applications in automotive and aerospace industries. However their applications are still limited due to several undesirable properties, such as relative low strength, low ductility and poor corrosion resistance.

Refining grains is an effective way to improve the comprehensive mechanical properties of magnesium alloys by two kinds of method. One is to add alloying elements such as Zr, Sr and Ca [1-3]. The addition of alloying elements in magnesium alloy can effectively refine grain size but may introduce other problems associated with formation of foreign particles, hot tearing, and drosses. The other is to use physical ways, which is always considered as a better one, such as severe plastic deformation [4-8] and physical vibration [9-13] during the solidification process of magnesium alloys.

Ultrasonic vibration is one of the simple and effective physical methods to refine grain size of magnesium alloys during solidification process [10-13]. Since the occurrence of acoustic cavitation and streaming in the liquid metal at certain sonication intensities, the process of ultrasonic vibration solidification treatment (UVST) significantly influences the microstructure, modifying such properties as, the grain size, the refinement of the β phase, the density of dislocations and twins. Many reports suggested that the corrosion behavior of magnesium alloy is significantly dependent on its microstructure [14-18]. How the above microstructural factors influence the corrosion behavior of AZ80 alloy is yet to be satisfactorily understood.

For better understanding the effect of ultrasonic vibration on the corrosion behaviour of AZ80 alloy, the aim of this work was to investigate the relationship between microstructure and the corrosion resistance of the AZ80-NS and AZ80-UVST alloy.

2. BACKGROUND: RECURRENCE PLOTS

Recurrence plots (RPs) are a valuable tool for assessing the geometry of the dynamics exploiting non-linear dependencies even in non-stationary time-series. These plots disclose distance relationships between points on a dynamical system providing a faithful representation of the time dependencies (correlations) contained in the data [19]. This is a graphical tool for the diagnosis of drift and hidden periodicities in the time evolution of dynamical systems, which are unnoticeable otherwise. Recurrence plots (RPs) are graphical tools elaborated by Eckmann et al. based on Phase Space Reconstruction [19]. The method of RPs is introduced to visualize the time dependent behavior of the dynamics of systems, which can be pictured as a trajectory in the phase space [20, 21]. It represents the recurrence of the m -dimensional phase space trajectory \vec{x}_i . They are a graphical representation of the $N \times N$ -matrix:

$$R_{i,j} = \Theta(\varepsilon - \|\vec{x}_i - \vec{x}_j\|), i, j = 1, 2, 3, \dots, N, \quad (1)$$

where $\vec{x}_i \in R^d$ stands for the point in phase space at which the system is situated at time i , ε is a state dependent cut-off distance (a predefined threshold), $\|\bullet\|$ is the norm of vectors, $\Theta(\cdot)$ is the Heaviside function and N is the number of states.

One assigns a “black” dot to the value one and a “white” dot to the value zero. The two-dimensional graphical representation of $R_{i,j}$ then is called a RP.

There are two different types of RPs: unthresholded recurrence plots (UTRP) and thresholded recurrence plots (TRPs), respectively. An unthresholded RP is not binary but its matrix $R_{i,j}^u$ is given by the (real valued) distances of the vectors \vec{x}_i and \vec{x}_j . The matrix then is usually represented in a two-dimensional colored plot. It has been shown that from an unthresholded RP it is possible to reconstruct time series [21]. However unthresholded RPs are more difficult to quantify than binary RPs. For this reason, in data analysis usually binary RPs is used.

The basic idea to keep in mind when studying RPs is simple: If the underlying signal is truly random and has no structure, the distribution of colors over the RP will be uniform, and so there will not be any identifiable patterns. On the other hand, if there is some determinism in the signal generator, it can be detected by a characteristic distinct distribution of colors. Considering this, the length of diagonal line segments of the same color on the UTRP can give an idea about the signal predictability. In UTRPs, hot colors (white, yellow, and orange) can be associated with small distances between vectors, while cold colors (blue, black) may be used to show large distances. In this way, it is possible to visualize and study (qualitatively) the motion of the system trajectories and infer some characteristics of the dynamical system that generated the time series.

Considering that the graphical presentation given by recurrence might be difficult to be evaluated visually, Zbilut and Webber [22] did propose a set of parameters which are part of the recurrence quantification analysis (RQA). In this work, we did consider the use of the following parameters of RQA:

The percent recurrence (%R), quantifies a percentage of the plot occupied by recurrent points. It quantifies the number of time instants characterized by a recurrence in the signals interaction: the more periodic the signal dynamics, the higher the %R value.

The percent determinism (%D), quantifies a percentage between the recurrent points that form upward diagonal line segments and the entire set of recurrence points. The diagonal line consists of two or more points that are diagonally adjacent with no intervening white space. This parameter contains the information about the duration of a stable interaction: the longer the interactions, the higher the %D value.

3. EXPERIMENTAL

3.1. Materials preparation

The percentage composition of the cast AZ80 alloy is 8.21% Al, 0.44% Zn and 0.19% Mn. The melting of AZ80 Mg alloy was carried out in a laboratory resistance furnace with an iron crucible and protected by CO₂ + 0.5% SF₆ atmosphere in order to prevent severe oxidation. The melt was overheated to 650 ± 10 °C and controlled at this temperature for 600 s. Then the preheated ultrasonic radiator was inserted into the magnesium alloy melt and the magnesium alloy melt was treated by the pulsed ultrasonic with the power of 150 W for 50 s and with the pulse width of 150 μs. The treated melt was water quenched immediately after the pulsed ultrasonic treatment. For comparison reasons, samples were also made without ultrasonic vibration.

All of the specimens were wet ground to a 1000-grit finish by abrasive paper, degreased with acetone, cleansed with distilled water and dried in a compressed hot air flow. The test solution was 3.5% sodium chloride in weight with magnesium hydroxide saturated prepared by analysis grade chemicals and distilled water.

3.2. Microstructure observation

The microstructure changes were characterized by scanning electronic microscopy (SEM QUANTA 200 F). The corrosion morphology was observed after the removal of corrosion products. The volume fraction of the β phase was measured from the recorded SEM images taken using software Photoshop 7.0.

The microstructure of specimens of the NS and UVST alloy was investigated by transmission electron microscopy (TEM) type TECNAI G² F3, with the work function of 300 kV. Specimens for TEM were cut from middle sections of the ingot. Thin foils for TEM were cut to about 500 μm by electron discharge cutter and later ground and polished on both sides to a thickness of about 70 μm . Then the thin foils were ion milled at room temperature in a Gatan PIPS with a small incident angle until perforation.

3.3. Weight loss measurements

The specimens were cut into coupons of dimensions 15 \times 10 \times 3 mm for immersion tests and more than five specimens used for each test for good reproducibility. The samples were weighted before exposure using a digital balance (Sartorius CP225D) with a precision of 0.0001 g for the original weigh. After immersion for 10 h in the test solutions with a bath temperature at 25 ± 1 °C, the corroded specimens were immersed in a chromate solution (200 g/L CrO₃ + 10g/L AgNO₃) solution for 5-10min to remove the corrosion products. Finally, the specimens were washed with deionized water, dried by hot air flow and reweighted to obtain the weight loss.

3.4. Electrochemical measurements

Potentiodynamic polarization and EIS were performed in a three-electrode cell, using a platinum foil as counter electrode and an Ag/AgCl (saturated by KCl) electrode as reference electrode.

The polarization measurements were carried out at a scan rate of 1 mV s⁻¹ and the starting potential was -0.3 V vs open circuit potential (OCP). The electrochemical impedance spectroscopy (EIS) measurement was carried out over a frequency ranging from 100 kHz to 10 mHz by using a 5mV amplitude sinusoidal voltage.

The localized electrochemical impedance spectroscopy (LEIS) measurements were performed through a M370 scanning electrochemical system, which was comprised of a M370 scanning control unit, a M273A potentiostat, a M5210 lock-in amplifier and a video camera system. The microprobe was stepped over a designated area of the electrode surface. The scanning took the form of a raster in

x - y plane. The step size was controlled to obtain a plot of 16×12 lines. The AC disturbance signal was 10mV, and the excitation frequency for impedance measurements was fixed at 1000 Hz.

Electrochemical noise (EN) measurements were performed using an Autolab electrochemical workstation equipped with electrochemical noise module. Two identical specimens were used as the working electrode (WE) and an Ag/AgCl (saturated by KCl) electrode as the reference electrode, respectively. The electrochemical current noise was measured as the galvanic coupling current between two identical WE kept at the same potential. EN data was simultaneously recorded with time for 10 h. Each set of EN records, containing 4096 data points, recorded with a data-sampling interval of 0.08 s. One hundred and ten records were analyzed for each specimen. Before EN analysis, the direct-current (DC) trend of raw noise was removed by means of modified MAR method [23].

4. RESULTS

4.1. Microstructure characterization

4.1.1. Scanning electron microscopy

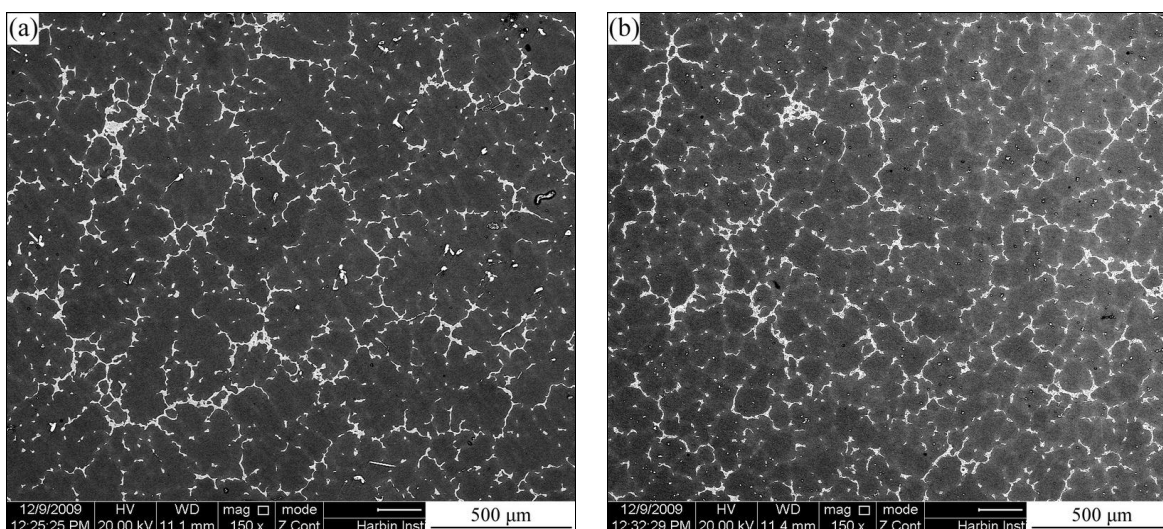


Figure 1. SEM images of (a) AZ80-NS and (b) AZ80-UVST alloy.

The microstructure of AZ80 alloy is altered considerably after the ultrasonic treatment (Fig. 1). For the AZ80-NS alloy, the coarse dendrites of the primary phase (α phase) are presented throughout the ingot, demonstrating the normal dendrite growth mode. With the application of ultrasonic treatment, because the dendritic structure is broken into finer globular one, AZ80-UVST alloy exhibited a more uniform microstructure, and the β phase segregated at the grain boundaries is thinner and smaller than AZ80-NS alloy (Fig. 1b)..

The volume fraction of the β phase of two alloys is calculated according SEM results by software. After UVST process, the volume fraction of the β phase decreases from 9.4 % (AZ80-NS) to 6.6 % (AZ80-UVST). Solidification is still a typical equilibrium process even with the ultrasonic

vibration. Hence, it is impossible to induce such significant difference on the volume fraction of the β phase for the AZ80 alloy with and without UVST. The only proper explanation for this contradictory result should be that many tinny particles of the β phase are not in the statistic due to the lower resolution of SEM. Therefore, in order to understand the effect of the ultrasonic vibration on the microstructure of AZ80 alloy, the TEM examination was done.

4.1.2. Transmission electron microscopy

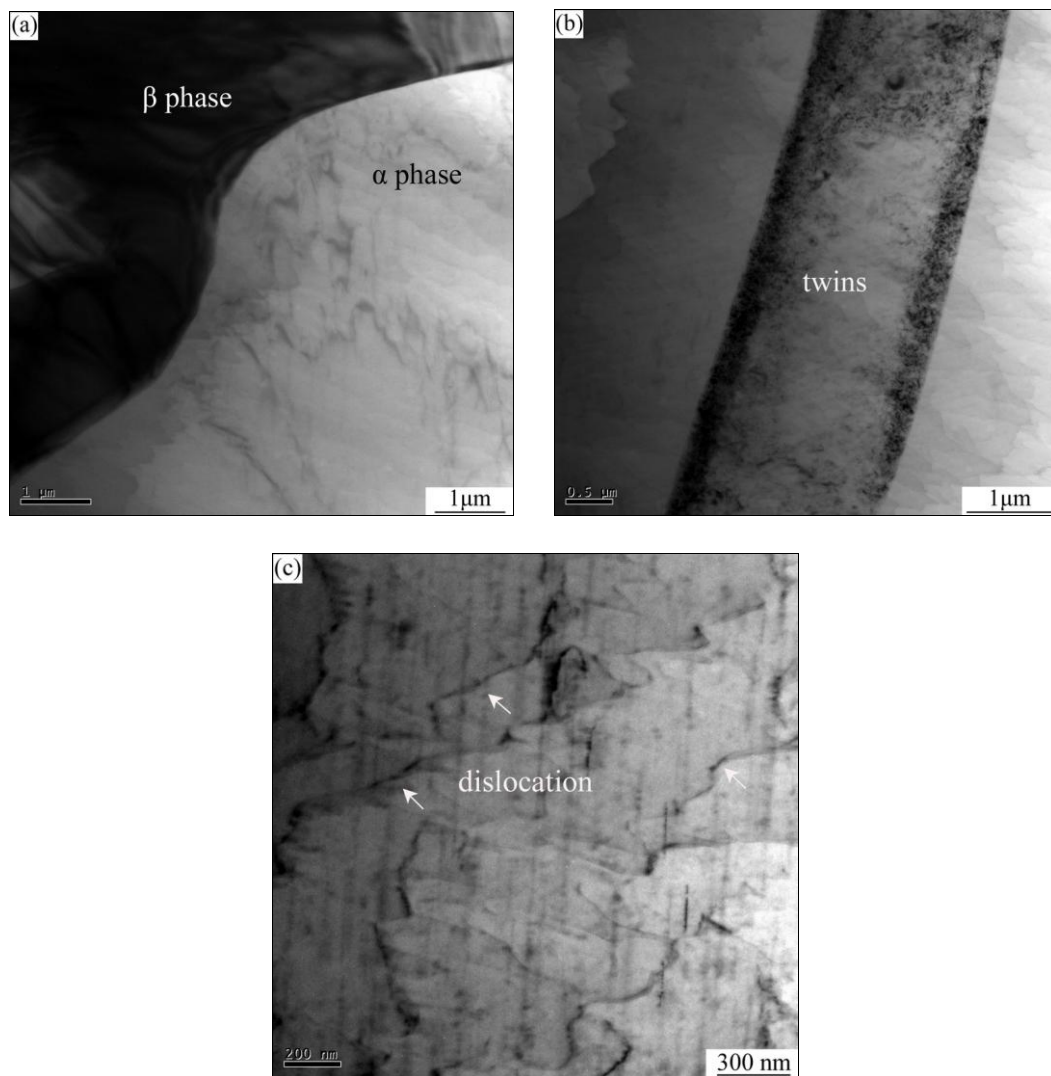


Figure 2. TEM images of AZ80-NS alloy. (a) grain boundary, (b) twins and (c) dislocations (white arrow).

The TEM images of AZ80-NS alloy presented in Fig. 2 reveal three key features: Firstly, a second phase is observed in the grain boundary (Fig. 2a). Secondly, twins are observed, although the volume fraction is not very high (Fig. 2b). Thirdly, the most of grains display the dislocations (Fig. 2c).

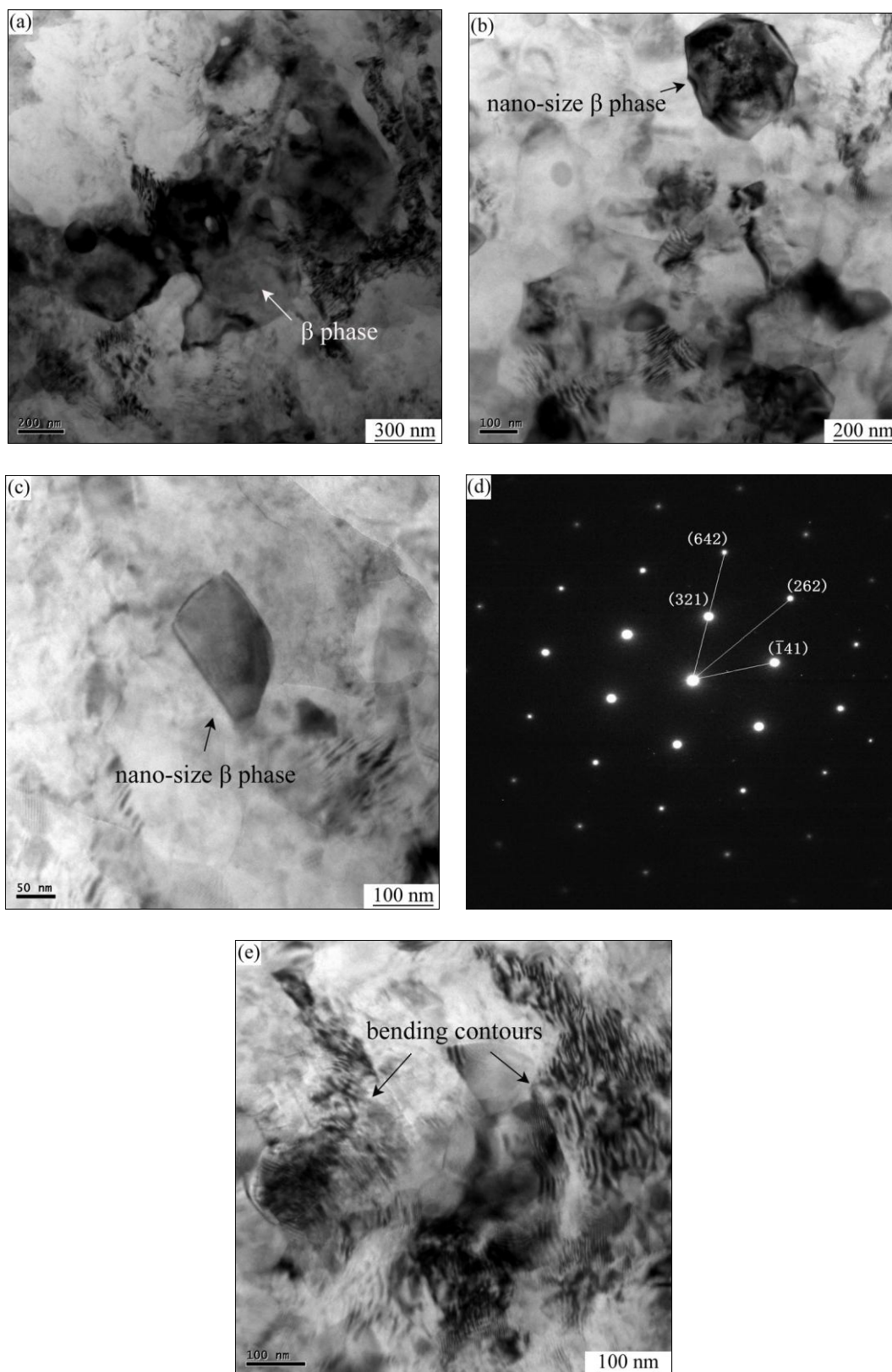


Figure 3. TEM images of AZ80-UVST alloy. (a) refined β phase, (b) and (c) nano-size β phase, (d) selected area diffraction, (e) bending contours.

There are remarkable changes on the microstructure after the UVST process. The second phase is refined, even is nanocrystallized. Some refined β phase precipitates along the grain boundary of the

α phase (Fig. 3a), which is similar to that of AZ80-NS alloy. The others polygon second phases with the size of about 100-200 nm disperse on the grain boundary (Fig.3 b, c), which is identified as $Mg_{17}Al_{12}$ phase by selected area diffraction (Fig. 3d). This observation supports clear evidence to the reasoning about volume fraction of the β phase, and indicates that volume fraction of nano-size β phase is high in the AZ80-UVST alloy. Moreover, due to the breakdown of dendritic structure by ultrasonic treatment, some matrix grains exhibit the large internal stresses, as indicated by the bending contours in the TEM images (Fig. 3e). However, as we can learn from Fig. 3, there is no evidence for twins and dislocations for AZ80-UVST alloy.

4.2. Corrosion measurements

4.2.1. Weight loss measurements

Table 1. Weight loss of AZ80-NS and AZ80-UVST alloy after 10 h of immersion.

	AZ80-NS	AZ80-UVST
Weight loss (g.m-2.h-1)	1.481	0.938

With respect to the determination of corrosion rate, the most accurate and precise method is probably the weight loss test. Average corrosion rates of AZ80-NS and AZ80-UVST alloy obtained from weight loss tests are shown in Table 1. It can be seen that the corrosion rate of AZ80-UVST alloy decrease down to $0.938 \text{ g m}^{-2} \text{ h}^{-1}$ compared with $1.481 \text{ g m}^{-2} \text{ h}^{-1}$ for AZ80-NS alloy, which indicates that UVST process improves the corrosion resistance of AZ80 magnesium alloy.

4.2.2. Polarization measurements

Table 2. Fitted parameters of polarization curves of AZ80-NS and AZ80-UVST alloy.

Specimen	$E_{\text{OCP}} (V_{\text{SHE}})$	$i_{\text{corr}} (\text{A.cm}^2)$
AZ80-NS	-1.512	1.421×10^{-5}
AZ80-UVST	-1.456	2.907×10^{-6}

The polarization curves of AZ80-NS and AZ80-UVST alloy are illustrated in Fig.4. The polarization curves are fitted and the corresponding results are shown in Table 2. The corrosion current, i_{corr} , of the AZ80-UVST alloy is lower than that of the AZ80-NS alloy, which indicates the UVST process decreases the corrosion rate of AZ80 alloy. Furthermore, the anodic polarization curves of AZ80-UVST alloy shifts to noble direction, implying the inhibition of anodic polarization behaviour; the cathodic polarization curve of two alloys is almost superposition, which indicates that UVST process has no influence on the hydrogen reduction mechanism.

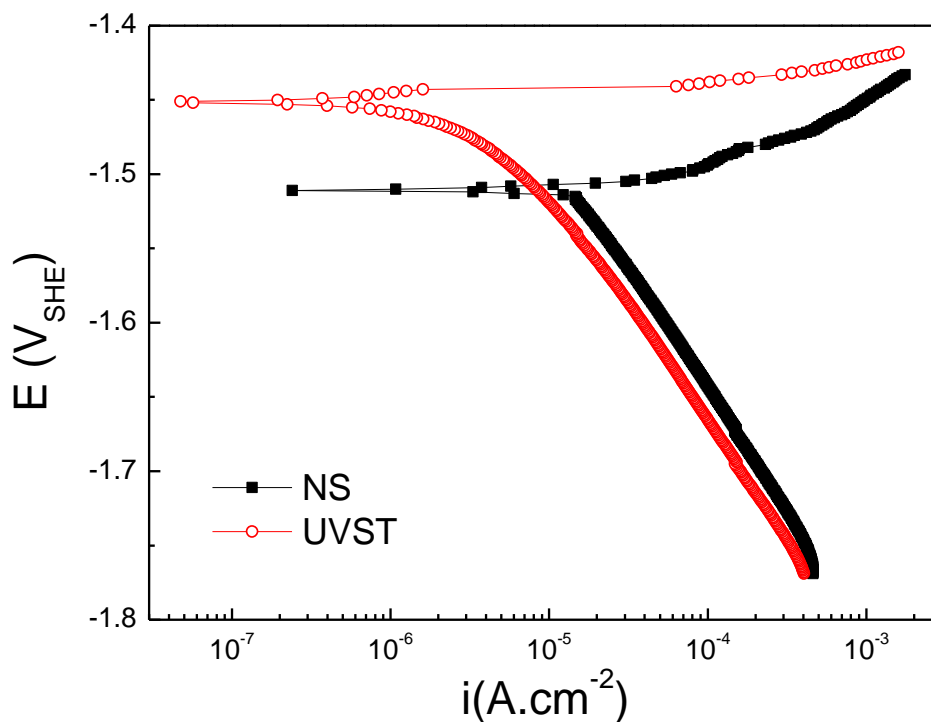


Figure 4. The polarization curves of AZ80-NS and AZ80-UVST alloy in 3.5% NaCl solution saturated by $\text{Mg}(\text{OH})_2$.

4.2.3. Local electrochemical impedance spectroscopy

LEIS maps for the AZ80-NS and AZ80-UVST alloy during a period of 10 h are given in Fig. 5. The maps clearly depict surface reactivity as reflected by the hill- or vally- like impedance fluctuation in the vertical Z direction. For LEIS map, a higher impedance value corresponds to a lower anodic activation zone and a lower impedance value represents a higher reactivity zone.

For the AZ80-NS alloy, in the initial stage of immersion, the impedance distribution illustrates un-uniform feature (Fig. 5 a), which attributes to the influence of Al since the corrosion rate of β phase appears lower than that of the α phase. With increasing immersion time, the impedance of AZ80-NS alloy remarkably decreased (Fig.5 b, c), which implies that the AZ80-NS alloy undergoes serious corrosion.

In general, AZ80-UVST alloy shows the higher impedance value level for all immersion periods comparing with that of AZ80-NS alloy. Localized corrosion is detected in zone X after 6h of immersion (Fig. 5e). With increasing immersion time, the localized corrosion in zones X disappears, while the corrosion in zones Y is detected (Fig. 5f), which indicates that the corrosion site on AZ80-UVST alloy shows high repassivation susceptibility and is hard to continuously develop. In the other word, AZ80-UVST alloy has higher corrosion resistance than AZ80-NS alloy, which is consistent with the results obtained from weight loss and polarization measurements very well.

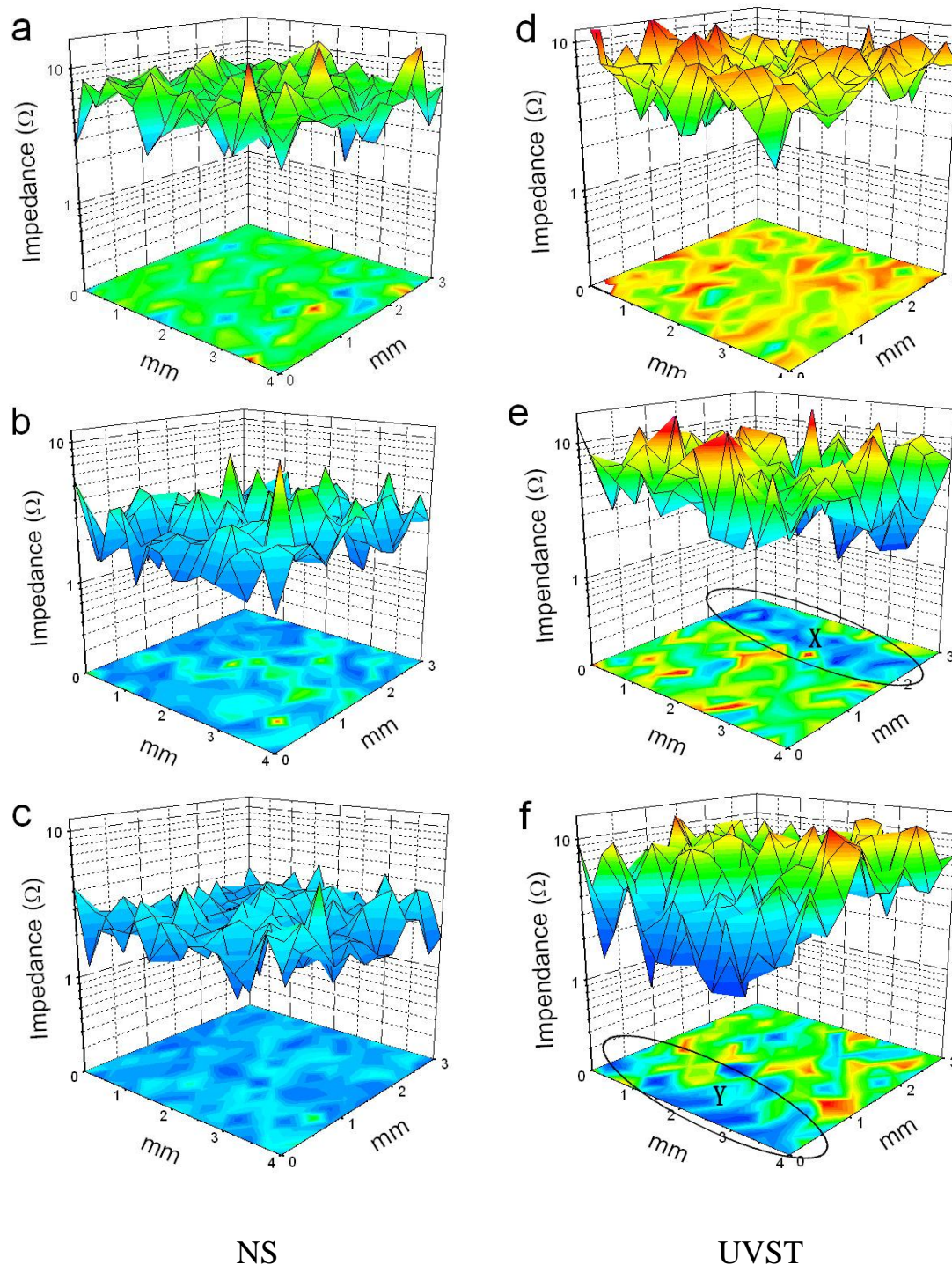


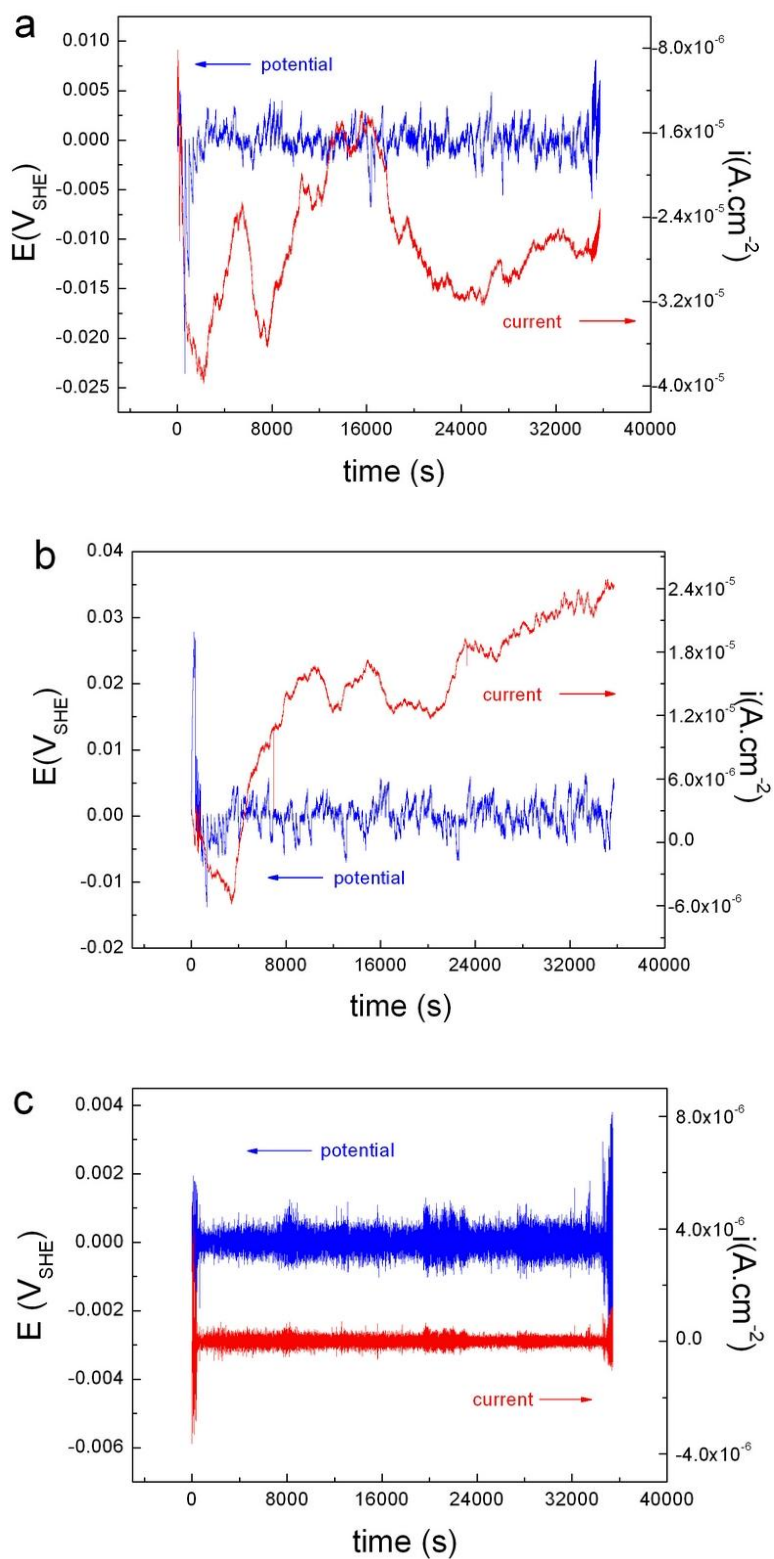
Figure 5. LEIS maps for the AZ80-NS and AZ80-UVST alloy in 3.5% NaCl solution saturated by Mg(OH)₂ after (a) and (d) 2 h, (b) and (e) 6h, (c) and (f) 10h of immersion.

4.2.4. Electrochemical noise

The raw and DC trend removal EN data of the AZ80-NS and AZ80-UVST alloy, during immersion for 10 h are shown in Fig. 6. The EN data is transformed from the time domain into the frequency domain by FFT. Spectral noise plot, $R_{sn}(f)$, is defined as:

$$R_{sn}(f) = \left| \frac{V_{PSD}}{I_{PSD}} \right|^{\frac{1}{2}} \quad (2)$$

where V_{PSD} and I_{PSD} are the potential and current PSD plots respectively.



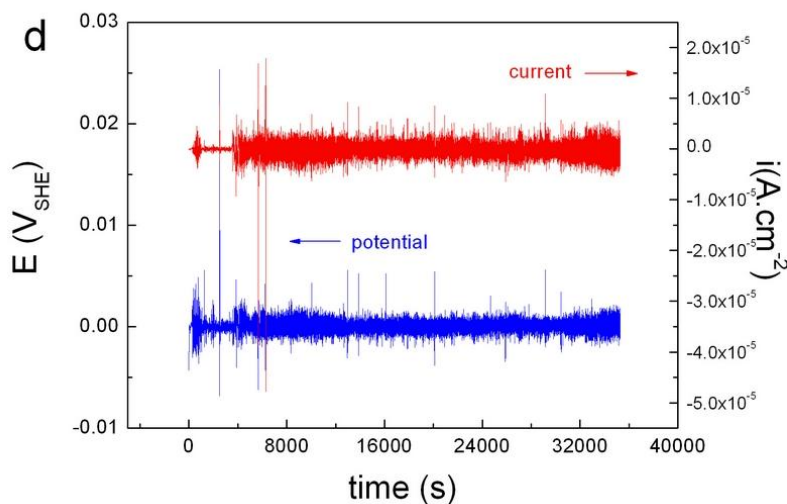


Figure 6. The raw and DC trend removal electrochemical noise of (a), (c) AZ80-NS and (b), (d) AZ80-UVST alloy.

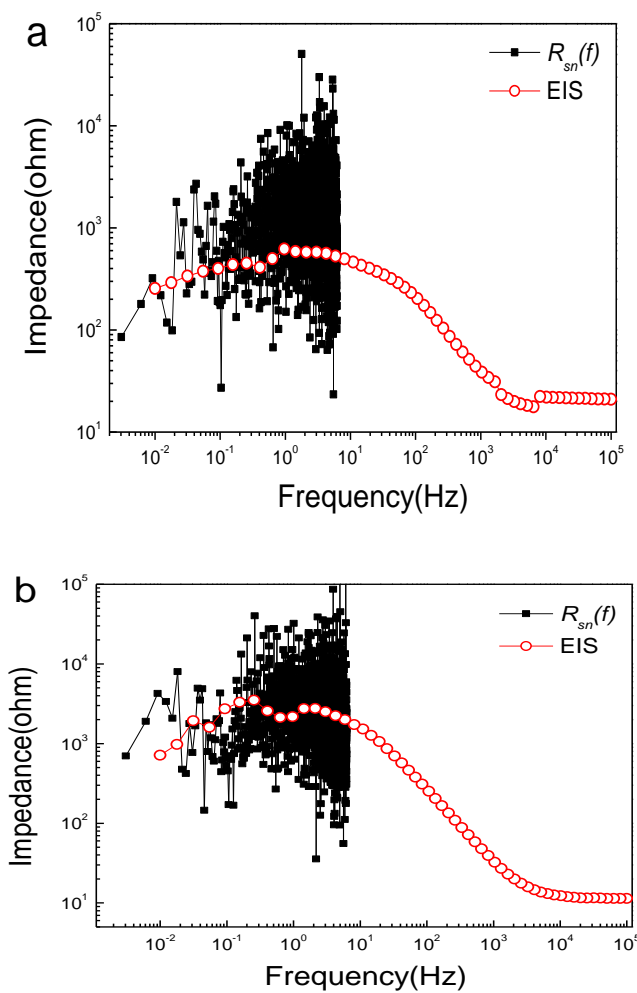


Figure 7. Comparison between spectral noise resistance, $R_{sn}(f)$, and EIS data.

The physical means of $R_{sn}(f)$ is the impedance in the low-frequency range [24]. In order to validate the reliability of EN data, EIS was carried out and compared with EN data. As presented in Fig. 7, for the two alloys, perfect superposition between the $R_{sn}(f)$ and Bode plot is observed, indicating the satisfactory reliability of the EN data.

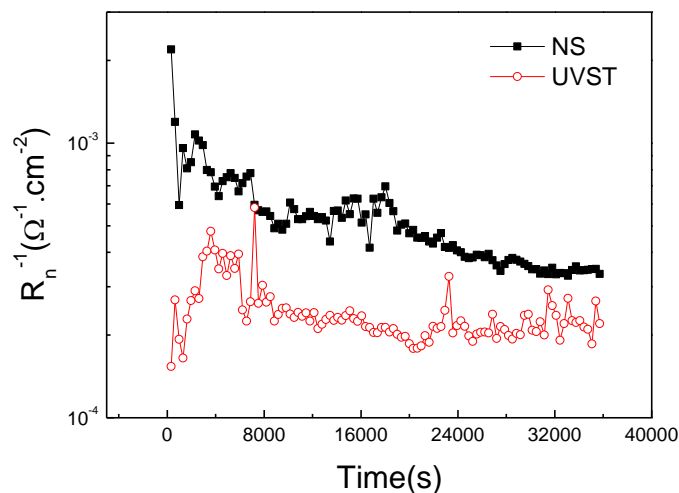
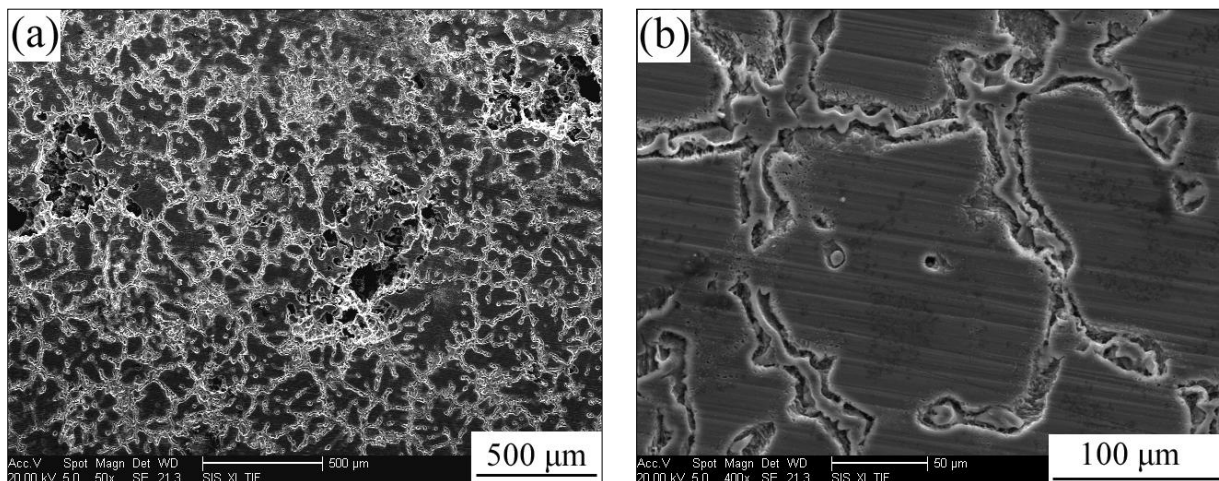


Figure 8. The reciprocal of R_n of AZ80-NS and AZ80-UVST alloy during the whole immersion period in 3.5% NaCl solution saturated by $\text{Mg}(\text{OH})_2$.

EN data analysis in the time domain involved the calculation of the electrochemical noise resistance R_n , defined as the ratio of a standard deviation of the potential to that of the current noise, which varied inversely with the corrosion rate [25-27]. Fig. 8 shows the reciprocal of R_n of the AZ80-NS and AZ80-UVST alloy, which suggests that AZ80-NS alloy exhibited higher corrosion rate than AZ80-UVST alloy during the immersion period.

4.3. Corrosion morphology



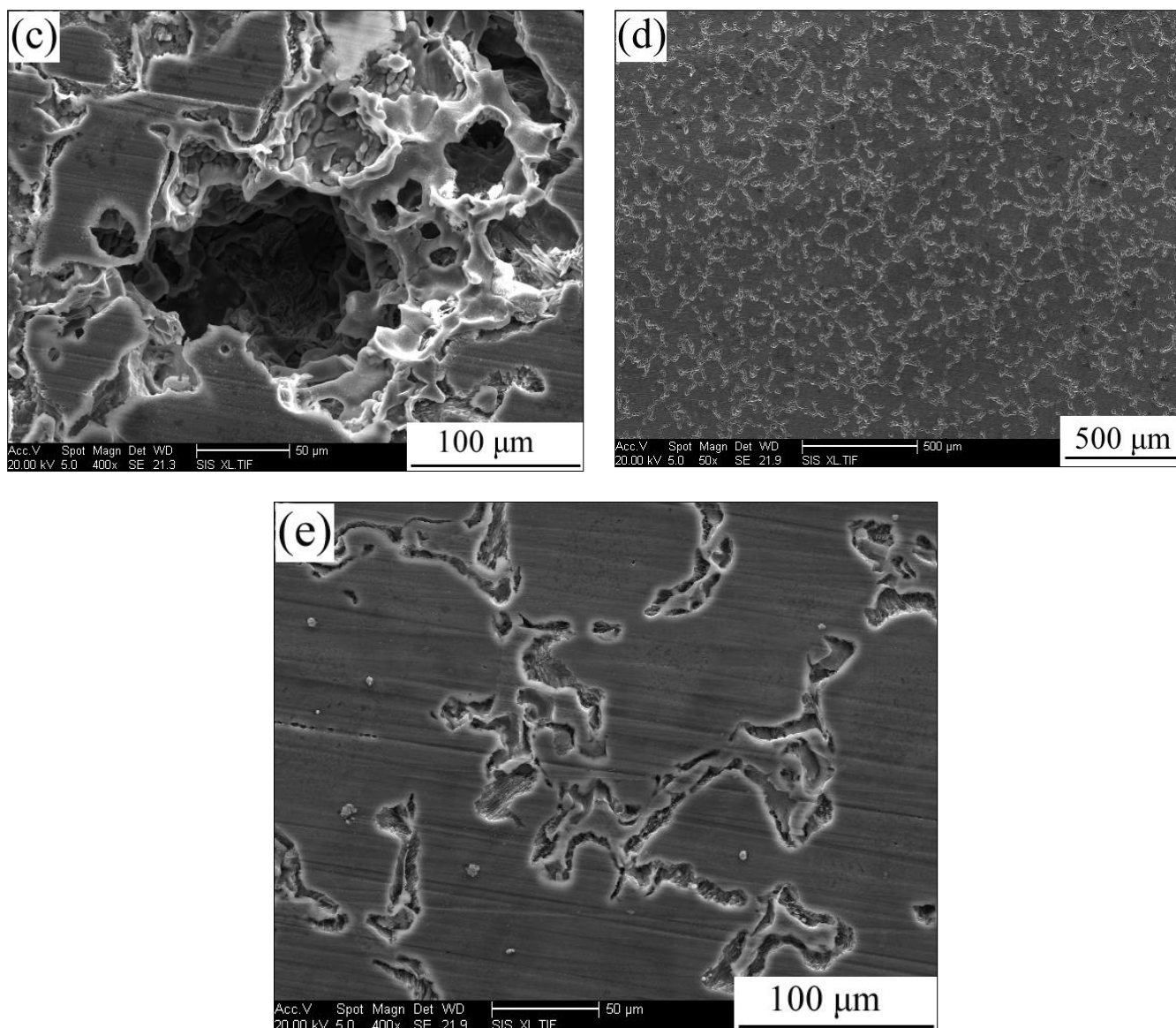
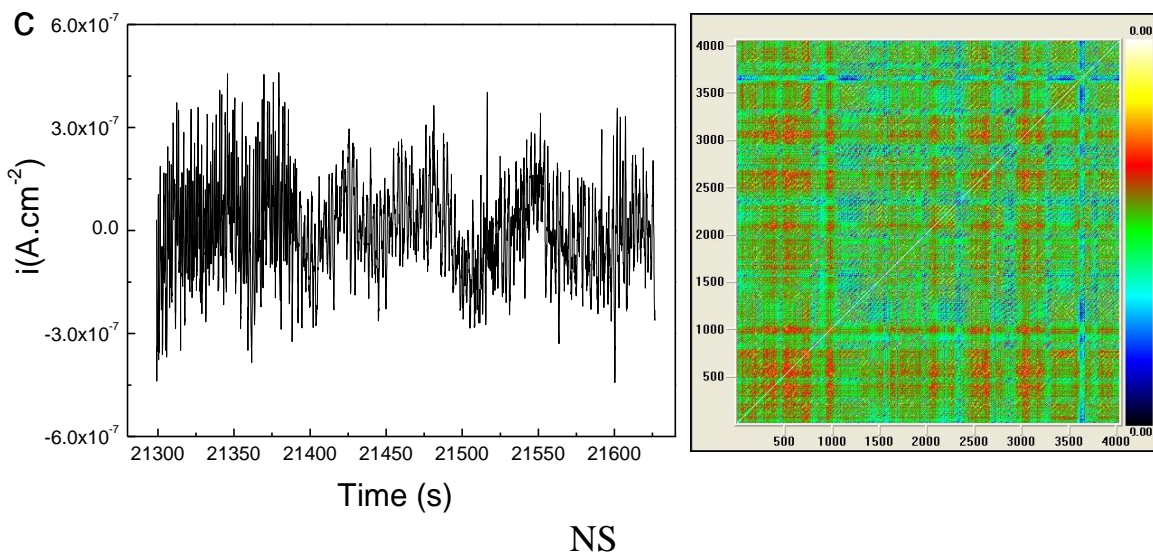
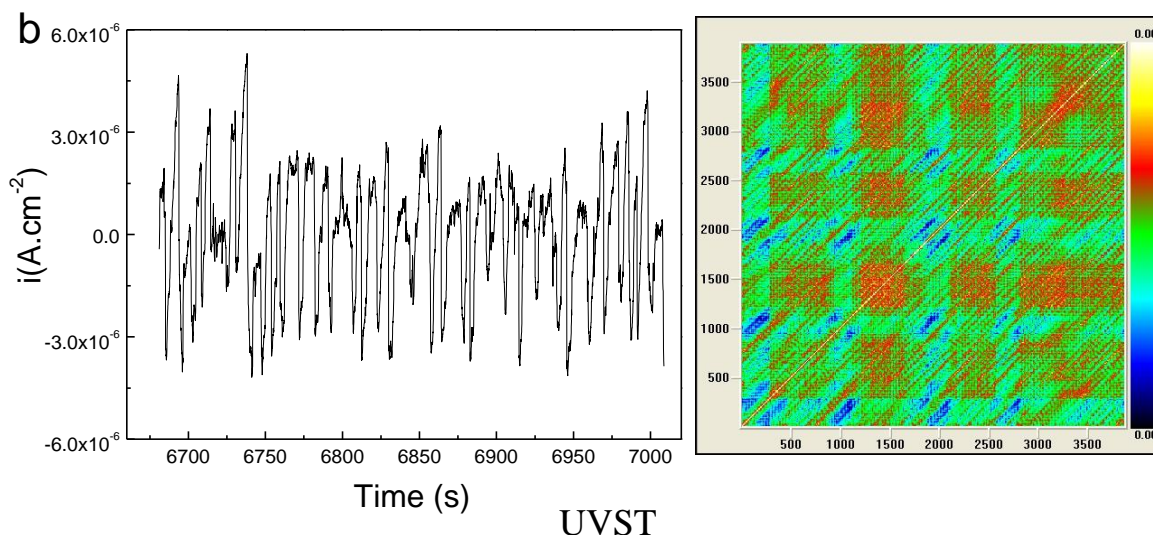
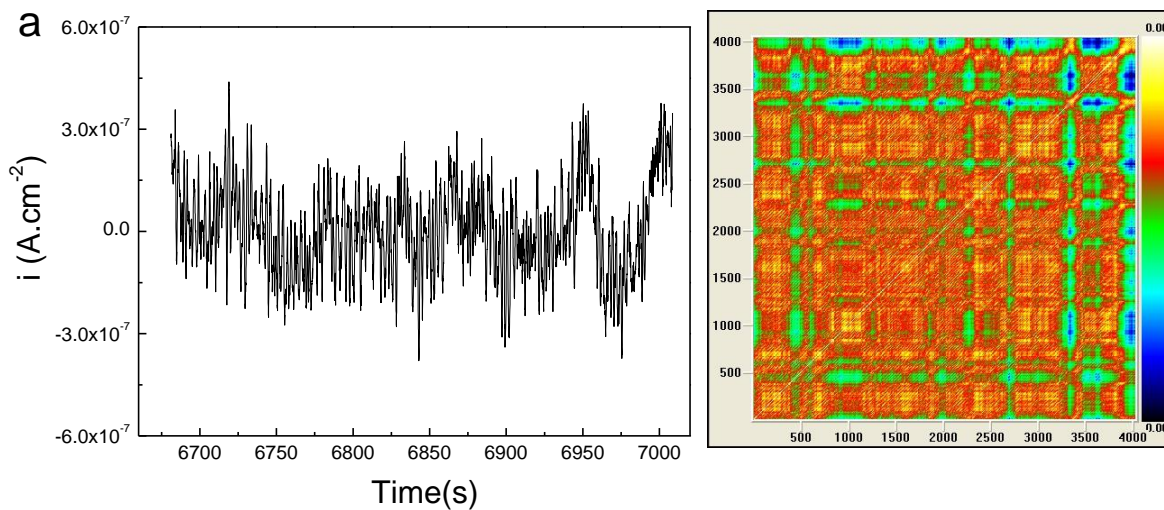


Figure 9. The corrosion morphology of AZ80-NS alloy with (a) low magnification and (b), (c) high magnification; the corrosion morphology of AZ80-UVST alloy with (d) low magnification and (e) high magnification.

The corrosion morphologies of two alloys after 10 h of immersion are shown in Fig. 9. For the AZ80-NS alloy, two kinds of corrosion morphologies are observed (Fig. 9a). Most of corroded surface shows typical micro-galvanic corrosion feature (Fig. 9b), furthermore, some pitting cavities are also observed (Fig. 9c). Comparing with AZ80-NS alloy, the nature of corrosion of the AZ80-UVST alloy seems to be remarkably different. The corrosion process was essentially micro-galvanic corrosion (Fig. 9 d, e). These observations again indicate that the corrosion resistance of AZ80 alloy is improved after UVST process.

5. DISCUSSION

5.1. Corrosion mechanism by means of EN analysis based on Recurrence Quantification Analysis



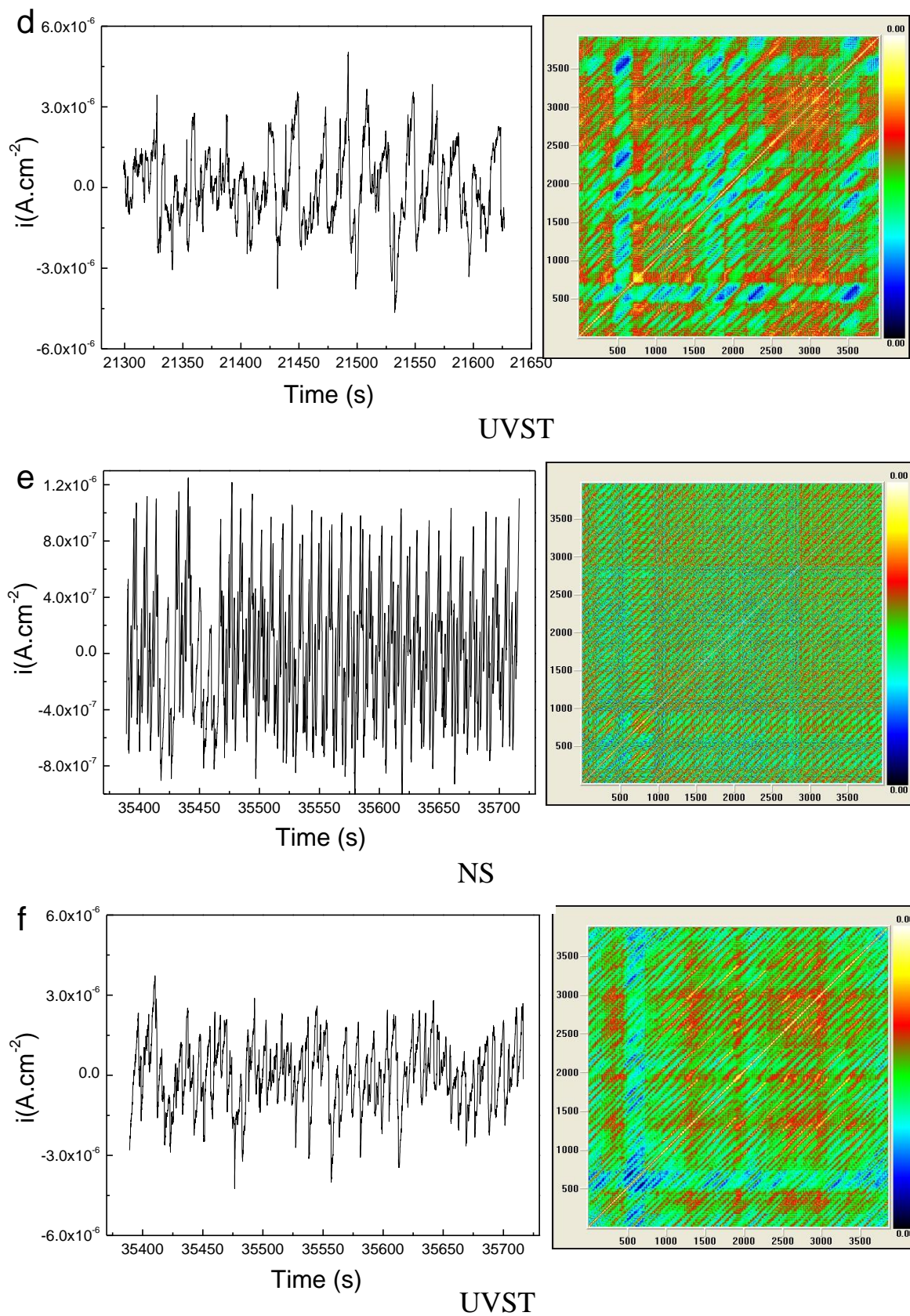


Figure 10. Recurrence plots of obtained from current noise time series with different immersion time (a) AZ80-NS, $t = 6681$ s; (b) AZ80-UVST, $t = 6681$ s; (c) AZ80-NS, $t = 21299$ s; (d) AZ80-UVST, $t = 21299$ s; (e) AZ80-NS, $t = 35389$ s; (f) AZ80-UVST, $t = 35389$ s;

A collection of electrochemical noise signals for two alloys and their respective Rps are shown in Fig. 10. All RPs are classified into categories depending upon the magnitude of the distance and color coded as follows: white and yellow pixels represent system states that are closest to each other in the reconstructed phase space, green pixels correspond to intermediate distances, while blue and black pixels represent still “recurrent states” but separated by even larger distances.

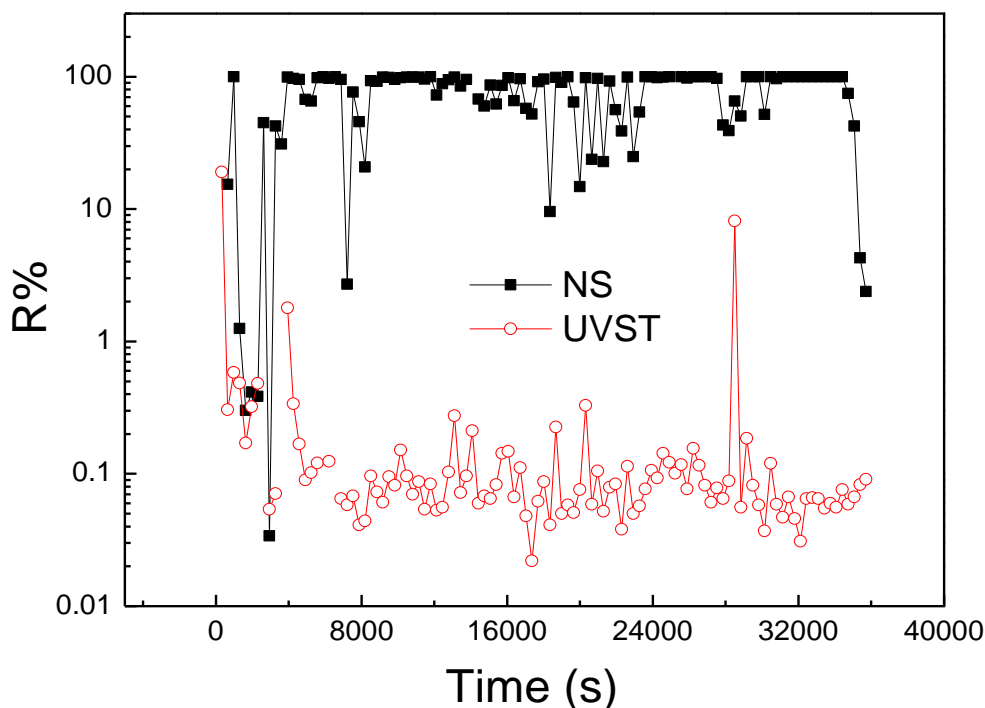


Figure 11. %R as a function of immersion time of AZ80-NS and AZ80-UVST alloy.

In order to obtain more information from RPs, a number of measures of complexity which quantify the small scale structures in RPs, has been proposed and are named as recurrence quantification analysis (RQA) [20, 21]. Among the quantities that are usually calculated in a RQA, the following parameters are considered in thin work: percent recurrence (%R), percent determinism (%D).

The %R value of the AZ80-NS and AZ80-UVST alloy are evaluated and presented in Fig. 11 as a function of the immersion time. As mentioned in the section 2.3, the more periodic the transient, the higher the %R value. Fig. 11 indicates that the %R value of the AZ80-NS alloy (average 75.13%) is far higher than that of AZ80-UVST alloy (average 0.28%), which implies that the EN transients of the AZ80-NS alloy are more periodic than that of the AZ80-UVST alloy. The higher periodicity of transients indicates higher generation frequency of transients, suggesting higher initiation rate of corrosion [28-30]. Fig.11 implies less metastable-corrosion generated on the AZ80-UVST alloy surface. In the other word, the UVST process decreases the initiation rate of metastable-corrosion of AZ80 alloy.

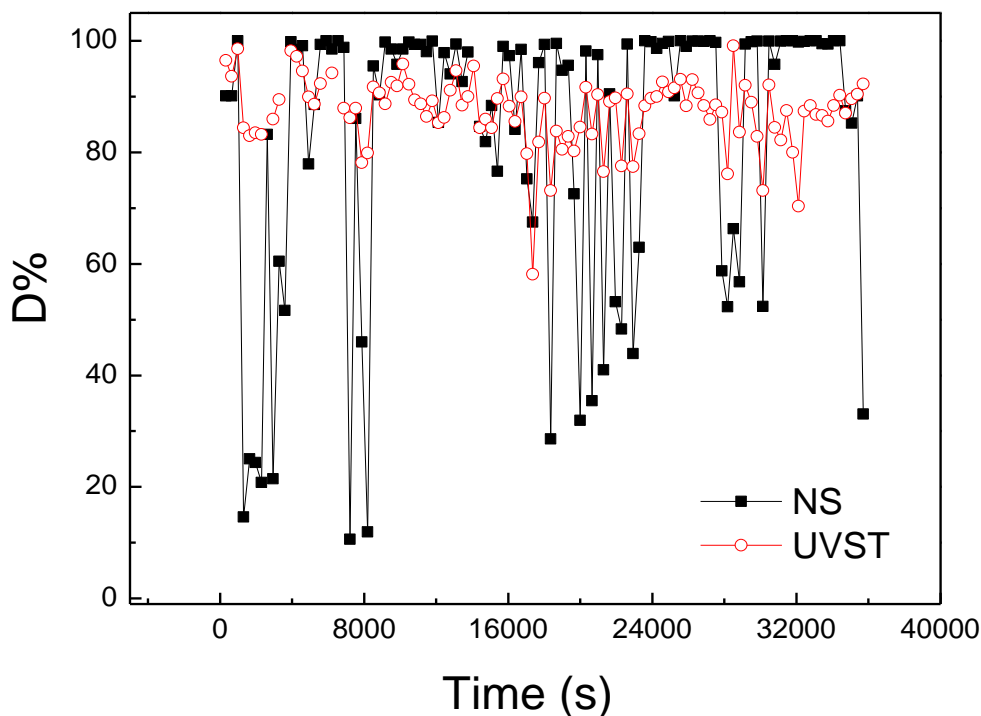


Figure 12. %D as a function of immersion time of AZ80-NS and AZ80-UVST alloy.

The percent determinism ($%D$), contained the information about the duration of a stable interaction: the longer the interactions, the higher the $%D$ value. Some researchers [28-30] further reveals that higher $%D$ value, the higher stable localized corrosion weight of all the corrosion events occurred on the metal surface. The $%D$ value of the AZ80-NS and AZ80-UVST alloy is illustrated in Fig.12. For the AZ80-NS alloy, $%D$ data points remains at higher value level (approximately 93.81%); while, for the AZ80-UVST alloy, the $%D$ value illustrates a lower level (about 87.33%), which indicates that the AZ80-UVST alloy has lower corrosion growth probability and the stable-corrosion is easier to generate on the AZ80-NS alloy surface than that of AZ80-UVST alloy.

Taking into consideration of the plots for both $%R$ and $%D$, AZ80-NS alloy not only shows higher corrosion initiation rate, but also has higher growth probability. Once a corrosion cavity generated, it is easy to become a stable one. This indicates lower corrosion resistance of AZ80-NS alloy, which is consistent with the results of weight loss and polarization measurements. Moreover, The RQA results also show good agreement with LEIS results. Owing to higher growth probability, many stable-corrosion generates on the AZ80-NS alloy surface, inducing the lower impedance level on the LEIS maps for all the immersion period (Fig.5 a, b, c). On the contrary, due to lower growth probability, the metastable-corrosion on the AZ80-UVST alloy surface is easier to be repassivation and is more difficult to become stable-corrosion, which presents a proper explanation why the corrosion on Zone X is repassivated during the immersion period (Fig.5 e, f).

5.2. The relationship between microstructure and corrosion behavior of AZ80-USVT alloy

According to the results of SEM and TEM, the microstructure variation of AZ80 alloy after USVT can be grouped into four categories: The first aspect is refinement and redistribution of the β

phase, the second one is the decrease of dislocations density and twins, the third one is the internal stress concentration of the partial matrix grains, and the last one is the refinement of grain size. By analyzing the relationship between the microstructure and corrosion behavior, the effect of UVST process on the corrosion behavior of AZ80 alloy can be discussed in the following issues:

5.2.1. Relationship between the microstructure and the corrosion initiation rate

The dislocations decrease the equilibrium potential of their vicinity [31, 32]. The decreasing equilibrium potential means the increase of over-potential between the equilibrium potential and open circuit potential, which implies the anodic dissolution current of magnesium alloy is accelerated according to the Battler-Volmer equation. Moreover, both the dislocation and twins are the crystallographic defects, and the distorted lattice in these sites can to some degree make the atom more susceptible to corrosion. Therefore, the combined effect of the decreased over-potential and defects implies that the matrix becomes stable and the corrosion site is not easy to be generated on its surface. In the other word, the decreased dislocations and twins inhibits the corrosion initiation rate of AZ80 alloy.

The effect of grain boundaries on the corrosion of magnesium alloy is still argued by the scientists [17, 32]. Some reporters suggest that the grain boundaries act as a physical corrosion barrier during for magnesium alloy [32]. The others disagree with this idea and imply that the grain boundaries in magnesium alloy are normally preferentially attacked by corrosion, and accelerated the corrosion rate [17]. In our opinion, the grain boundaries is a kind of crystallographic defect with three dimensions; to some degree, grain boundaries can be regarded as a dislocations wall between grains. Due to higher corrosion susceptibility of dislocations, the grain boundaries consisting of higher dislocations are impossible to acts as a “corrosion barrier”. Therefore, the grain boundaries should increase the corrosion initiation rate of magnesium as well as the dislocations and twins.

The influences of internal stress on the corrosion initiation rate can be understood based on two theories. On one hand, the stress concentration induces the breakdown of passive film [33]. On the other hand, the stress concentration increases the anodic dissolution activity of metals due to the mechano-chemistry effect [34]. Hence, the concentration of internal stress increases the corrosion initiation rate of magnesium.

Based on the above discussion, it can be seen that microstructural variation has two aspects of influence on the corrosion initiation rate of AZ80 alloy. The inhibition influence is attributed to the decreased dislocations and twins; meanwhile, the corrosion initiation rate is also accelerated by the increased volume of grain boundaries and internal stress concentration (acceleration influence). It seems that the inhibition influence on the corrosion initiation rate is greater than acceleration influence. Therefore, UNST decreases the corrosion initiation rate of AZ80 alloy. This is the reasonable reason why the anodic polarization curve of AZ80-UVST shifts to noble direction (Fig. 4), and the %R value of AZ80-UVST maintain at a lower level for all immersion period (Fig. 11).

5.2.2. Relationship between the refinement of the β phase and the corrosion growth

After the initiation of corrosion, the corrosion growth of magnesium alloy is determined by two issues [16]: 1) the cathodic reduction rate of the β phase. The cathodic process of magnesium is mainly dominated by hydrogen reduction process. Higher cathodic reduction rate leads to faster hydrogen evolution rate, which indicates the acceleration of corrosion. 2) The distribution of the β phase. The β phase plays as a barrier phase on the corrosion of magnesium alloy when it distributes continuously in the magnesium alloy. Otherwise, the β phase acts as cathode phase and accelerates the corrosion.

The cathodic reduction current on the β phase can be simply expressed as:

$$I_c = \theta_\beta \cdot i_{0,H} \exp\left(\frac{E_{OCP} - E_{e,H}}{\beta_{c,H}}\right) \quad (3)$$

where I_c is cathodic reduction current on the β phase, $i_{0,H}$ is exchange current density of hydrogen, θ_β is the volume fraction of the β phase, E_{OCP} is the open circuit potential, $E_{e,H}$ is the equilibrium potential of hydrogen, β_c is Tafel slope of hydrogen reduction. The E_{OCP} of the AZ80-UVST alloy is more noble than that of AZ80-NS alloy (Fig.4), indicating the decrease of the over-potential ($E_{OCP} - E_{e,H}$). If assumed the θ_β , $E_{e,H}$, $i_{0,H}$ and β_c were constant, the cathodic reduction current, I_c , would be decreased according to Eq.(3), which indicates that UVST does not influence the cathodic reduction mechanism, but decreases the hydrogen reduction rate.

The β phase acts as either a corrosion barrier or a galvanic cathode on the anodic process of AZ80-NS alloy [16]. From the point of view of barrier phase, the β phase grains of AZ80-UVST alloy are obviously refined and its distribution is more net-like than that of AZ80-NS alloy (Fig. 1). Hence, the refined β phase of AZ80-UVST alloy will be a much more effective barrier against anodic dissolution compared to that of AZ80-NS alloy. Accordingly, the corrosion on the AZ80-UVST alloy is hard to spread over the alloy surface and the corrosion growth probability is decreased.

From the point of view of cathode phase, the nano-size β phase particles with the higher volume fraction discontinuously precipitate on the grain boundaries after UVST process. The interface length between the α and β phase should be far longer than that of AZ80-NS alloy. Assuming the interface length as $L_{\alpha/\beta}$ and the galvanic distance of α phase as d , the average galvanic current of anodic polarized α phase on the unit area, \bar{i}_α , can be described as:

$$\bar{i}_\alpha = \frac{I_c}{L_{\alpha/\beta} \times d} \quad (4)$$

If the galvanic distance, d , for both alloys was same.

Due to:

$$I_{c,UVST} > I_{c,NS} \quad (5)$$

$$L_{\alpha/\beta,UVST} \gg L_{\alpha/\beta,NS} \quad (6)$$

Combined with Eq. (5) and (6):

$$\overline{i_{\alpha,UVST}} \ll \overline{i_{\alpha,NS}} \quad (7)$$

Owing to the lower average galvanic current, the metastable-corrosion site on the AZ80-UVST alloy surface shows a lower dissolution rate and is more difficult to form a larger cavity within a short period; meanwhile, the localized solution in the corrosion cavity is easier to be diluted by the bulk solution, which implies that the metastable corrosion on the AZ80-UVST alloy has the higher repassivation susceptibility.

Whether based on the barrier phase or cathode phase theory, the discussion results show good agreement with each other. The refined β phase of AZ80-UVST alloy induces the decrease of corrosion growth probability indeed. The reasoning is supported by Fig. 9, where only micro-galvanic corrosion is observed (Fig. 9d), whereas the AZ80-UVST alloy surface manifests both micro-galvanic corrosion and pitting corrosion feature (Fig. 9a). Moreover, these discussions are also consistent with the results obtained from EN analysis that the $D\%$ of AZ80-NS alloy is higher than that of AZ80-UVST alloy.

6. CONCLUSION

All the corrosion test results indicate that UVST process has strong influences on the corrosion behavior of AZ80 alloy. The relationship between microstructure and corrosion behavior of AZ80 alloy is founded. Its effect can be concluded as three issues:

(1) Weight loss, polarization and LEIS results reveal that the corrosion resistance of AZ80 alloy is improved by UVST process. The EN results analyzed by RQA indicate that the UVST process decrease both the corrosion initiation rate and its growth probability. The metastable-corrosion on AZ80-UVST alloy surface is more difficult to generate and develop to stable one than that on AZ80-NS alloy surface.

(2) UVST refines the grain matrix, induces the internal stress concentration, and obviously decreases its dislocation and twins. The increased grain boundary and the concentration of internal stress accelerate the corrosion initiation rate, while, the decreased dislocations and twins inhibit it. The decrease of the twins and dislocation density is the main factor, which implies the decrease of corrosion initiation rate.

(3) After UVST process, the refined β phase acts as key role on the corrosion growth process. On one hand, the hydrogen reduction rate on β phase is remarkably decreased due to the noble shift of E_{OCP} , which decrease the total quantity of electron transfer. On the other hand, the presence of refined and nano-size β phase significantly decreases the anodic polarization behaviour. The combined effect of these two factors indicates the decrease of corrosion growth probability.

ACKNOWLEDGEMENT

The authors wish to acknowledge the financial support of the program for New Century Excellent Talents in University of China (NCET-09-0052).

References

1. B. Kondori, R. Mahmudi, *Mater. Sci. Eng. A* 527 (2010) 2014
2. J. Zhou, J. Wang, J. Wang, Y. Yang, *Trans. Nonferrous. Met. Soc. China*, 20 (2010) s331
3. J. Chang, X. Guo, S. He, P. Fu, L. Peng, W. Ding, *Corros. Sci.* 50 (2008) 166
4. Q. Wang, Y. Chen, M. Liu, J. Lin, H. Roven, *Mater. Sci. Eng. A* 527 (2010) 2265
5. C. Fan, D. Chen, A. Luo, *Mater. Sci. Eng. A* 519 (2009) 38
6. H. Ding, L. Liu, S. Kamado, W. Ding, Y. Kojima, *J. Alloy. Compound* 456 (2008) 400
7. T. Liu, S. Wu, S. Li, P. Li, *Mater. Sci. Eng. A* 460-461 (2007) 499
8. G. Garces, F. Domínguez, P. Pérez, G. Caruana, P. Adeva, *J. Alloy. Compound* 422 (2006) 293
9. C. Fang, X. Zhang, H. Hao, S. Ji, J. Jin, *J. Mater. Sci. Technol.* 23 (2007) 806.
10. D. Gao, Z. Li, Q. Han, Q. Zhai, *Mater. Sci. Eng. A* 502 (2009) 2
11. M. Aghayani, B. Niroumand, *J. Alloy. Compound* 509 (2011) 114
12. Z. Zhang, Q. Le, J. Cui, *Trans. Nonferrous. Met. Soc. China*, 18 (2008) s113
13. M. Qian, A. Ramirez, A. Das, D. StJohn, *J. Cryst. Growth* 312 (2010) 2267
14. M. Ben-Haroush, G. Ben-Hamu, D. Eliezer, L. Wagner, *Corros. Sci.* 50 (2008) 1766
15. A. Pardo, M.C. Merino, A.E. Coy, F. Viejo, R. Arrabal, S. Feliú, *Electrochim. Acta* 53 (2008) 7890
16. G. Song, A. Atrens, M. Dargusch, *Corros. Sci.* 41 (1999) 241
17. G. Song, Z. Xu, *Electrochim. Acta* 55 (2010) 4148
18. G. Song, A. Bowles, D. StJohn, *Mater. Sci. Eng. A* 366 (2004) 74
19. J. Eckmann, S. Kamphorst, D. Ruelle. *Europhys. Lett.* 4 (1987) 973.
20. J. Zbilut, C. Webber. *Phys. Lett. A*, 171(1992) 199.
21. G. McGuire, N. Azar, M. Shelhamer, *Phys. Lett. A*, 237(1997) 43
22. C. Webber, J. Zbilut, *J. Appl. Physiol.* 76 (1994) 965
23. X. Liu, T. Zhang, Y. Shao, G. Meng, F. Wang, *Corros. Sci.* 52 (2010) 892
24. F. Mansfeld, C. Lee, G. Zhang, *Electrochim. Acta*, 43 (1998) 435
25. A. Lafront, W. Zhang, S. Jin, R. Tremblay, D. Dubé, E. Ghali, *Electrochim. Acta* 51 (2005) 489
26. J. Chen, W. Bogaerts, *Corros. Sci.* 37 (1995) 1839.
27. C. Gouveia-Caridade, M.I.S. Pereira, C.M.A. Brett, *Electrochim. Acta*, 49 (2004) 785.
28. E. Cazares-Ibáñez, G.A. Vázquez-Coutiño, E. García-Ochoa, *J. Electroanal. Chem.* 583 (2005) 17
29. E. García-Ochoa, J. González-Sánchez, N. Acuña, J. Euan, *J. Appl. Electrochem.* 39 (2009) 637.
30. N. Acuña-González, E. García-Ochoa, J. González-Sánchez, *Int. J. Fatigue* 30 (2008) 1211
31. G. Ben-Hamu, D. Eliezer, L. Wagner, *J. Alloy. Compound* 468 (2009) 222
32. N. Aung, W. Zhou, *Corros. Sci.* 52 (2010) 589.
33. R. Staehle, *Corros. Sci.* 49 (2007) 7
34. J. Ma, B. Zhang, J. Wang, G. Wang, E. Han, W. Ke, *Corros. Sci.* 52 (2010) 2867